metals

MDPI

Article

Increasing Wear Resistance of Low-Carbon Steel by Anodic Plasma Electrolytic Sulfiding

Tatiana Mukhacheva [1,2,*], Sergei Kusmanov [2], Igor Suminov [1], Pavel Podrabinnik [1], Roman Khmyrov [1] and Sergey Grigoriev [1]

[1] Department of High-Efficiency Machining Technologies, Moscow State University of Technology "STANKIN", 127994 Moscow, Russia
[2] Department of Mathematical and Natural Sciences, Kostroma State University, 156005 Kostroma, Russia
* Correspondence: mukhachevatl@mail.ru; Tel.: +7-9101979388

Abstract: The paper considers the problem of increasing the wear resistance of steel products. For the first time, the technology of anodic plasma electrolytic sulfiding is proposed to increase the wear resistance of low-carbon steel. The composition, structure, and frictional properties of modified surface layers after sulfiding have been studied. The type and mechanism of wear are determined. The influence of the sliding speed of the sample over the counter body on the friction and wear resistance of the samples after processing is analyzed. The possibility of saturation of low-carbon steel with sulfur in an electrolyte with sulfur compounds is shown. The iron sulfide FeS in the surface layer is found. It has been established that the thickness of the sulfide zone and the relative amount of FeS in it have a positive effect on reducing the coefficient of friction and mass wear. The greatest decrease in the friction coefficient by 5.5 times and weight wear by 64 times occurs after sulfiding at 500 °C for 10 min. It was found that the mechanism of wear of sulfided samples is fatigue wear during dry friction and plastic contact.

Keywords: plasma electrolytic treatment; steel; sulfiding; wear resistance; friction coefficient

Citation: Mukhacheva, T.; Kusmanov, S.; Suminov, I.; Podrabinnik, P.; Khmyrov, R.; Grigoriev, S. Increasing Wear Resistance of Low-Carbon Steel by Anodic Plasma Electrolytic Sulfiding. *Metals* **2022**, *12*, 1641. https://doi.org/10.3390/met12101641

Academic Editor: Kuan-Jen Chen

Received: 5 September 2022
Accepted: 25 September 2022
Published: 29 September 2022

1. Introduction

The increase in durability and reliability of machines, technological equipment, and tools is directly related to the increase in wear resistance [1–7]. One of the ways to reduce the friction coefficient and improve the running-in of parts in friction pairs is the chemical–thermal treatment of metal surfaces. There are many ways of chemical–thermal treatment of metals and alloys. One of these methods is anodic plasma electrolytic treatment (PET).

PET is a high-speed processing method. The heating rate to the required temperature is hundreds of degrees per second. The duration of diffusion saturation takes only a few minutes with the possibility of quenching in the same electrolyte without reheating. An important feature of high-speed heating is the reduction in the size of austenitic grains and the grinding of blocks inside the grain, which increases its diffusion susceptibility. The formation of diffusion layers is accelerated. High cooling rates make it possible to obtain martensite of increased tetragonality [8,9].

The processes of diffusion saturation with nitrogen, carbon, and boron have been largely studied under PET conditions. It is shown that the wear resistance of T8 steel increases by 18 times after cathodic plasma electrolytic carburizing [10]. On the friction tracks of untreated samples, there are scratches in the direction of the counter body sliding, characteristic of abrasive wear, and significant flaking-off of the material. There are areas with a high content of oxygen and zirconium, which indicates adhesion with a counter body of ZrO_2. Samples carburized in glycerin electrolyte are characterized by narrower and less deep friction tracks with much lower oxygen and zirconium content. Fatigue cracks have also been identified here. The conclusion is made about the transformation of abrasive wear into oxidative and fatigue wear.

Cathodic nitriding of S0050A steel in urea solution leads to a slight increase in the dry friction coefficient from 0.37 for an untreated sample to 0.4 for a nitrided sample at 600 °C for 5 min [11]. The friction coefficient also increases from 0.109 to 0.125 upon the application of friction with a lubricant by a tungsten carbide ball, probably due to an increase in surface roughness. Nevertheless, an increase in surface hardness leads to a decrease in volumetric wear during dry friction by about 3 times. Cathodic nitriding of 34CrNiMo alloy steel in a solution of carbamide (30%) and sodium carbonate (15%) reduces the intensity of adhesive wear of steel by 35% with dry friction of a corundum ball compared to untreated steel [12]. A similar treatment of nitrided SACMI steel using a 25% solution of potassium carbonate in formamide reduces weight wear by 15–20% compared to gas nitriding in dry friction with a counter body made of hardened steel [13]. Adhesive wear is also reduced after the cathodic nitriding of 38CrMoAl steel due to the formation of a needle-like structure containing nitrides, fine grains of cementite, and martensite [14].

Anodic nitriding increases the wear resistance of 40Ch steel in dry friction with a counter body made of sintered titanium carbide [15]. Wear tests of 40Ch steel under friction with grease on a steel disc hardened to 50 HRC after anodic nitriding in a solution of ammonia and ammonium chloride showed that wear is minimal at a temperature of 650 °C, when the minimum surface roughness and the highest hardness of the nitride–martensitic layer of 780 HV are reached [16].

The wear resistance of low-carbon steel after anodic nitrocarburizing in a solution of ammonium nitrate, glycerin, and ammonium chloride increases by 14 times [17]. An increase in temperature from 750 to 950 °C leads to a decrease in weight wear. The increase in wear resistance is associated with a concomitant increase in the hardness of the layer from 600 to 880 HV and a decrease in the friction coefficient from 0.15 to 0.12, despite an increase in surface roughness from 0.46 to 0.91 μm.

The wear resistance of H13 steel increases by 12 times after cathodic boriding in a solution containing borax and sodium hydroxide [18]. Anodic boriding in an aqueous solution containing 3% sodium tetraborate and 10% sodium hydroxide leads to an increase in the wear resistance of medium-carbon steel by an order of magnitude [19]. Wear tests of medium-carbon steel samples after they were borided in an aqueous solution of boric acid (5%) and ammonium chloride (10%) showed that the friction coefficient is always lower than that of the control sample, both with lubrication and with dry friction on a disk of hardened steel with a hardness of 50 HRC [20]. The minimum friction coefficient, equal to 0.13, and the greatest increase in wear resistance (16 times) is observed after boriding at 850 °C, when the highest values of microhardness and boron concentration in the layer are reached.

A positive result after cathodic PET was noted for saturation of low-carbon steel S12 with nitrogen and sulfur in a solution containing 60% urea and 5% sodium thiosulfate [21]. The treatment provides a 1.7-fold reduction in the friction coefficient and a 2-fold reduction in the width of the friction track.

All the above results convincingly demonstrate the significant potential of PET as a way to increase the wear resistance of steels and alloys, but the tribological picture does not appear to be studied. It is required to vary the test conditions over a wider range.

Of the numerous characteristics of surface roughness, only the average value of the profile irregularities Ra is usually used. However, with the same average roughness, the smoothing height and the set of step characteristics of the rough profile can differ significantly and affect the frictional properties in completely different ways. Therefore, a more informative complex roughness parameter should be used.

It is known that saturation of the surface of steel workpieces with sulfur allows for reducing the coefficient of friction and improving the wear-in of parts in friction pairs. To date, there have been no studies of the structure and properties of PET sulfided steels and their tribological properties under various test conditions.

Therefore, in this work, the possibility of saturation of the surface of low-carbon steel with sulfur during anodic PET–plasma electrolytic sulfidation (PES) is studied. The wear

mechanism of steel samples after PES is investigated when the sliding speed of the sample along the counter body varies within wide limits. The type and mechanism of wear are determined. The type of destruction of the friction bond during testing is revealed, the effect of the sliding speed on the nature of the interaction of surfaces in the contact zone is established, and the relationship of the structure of the sulfided layer and the properties of samples with the parameters of the friction process is studied.

2. Materials and Methods

2.1. Sample Processing

PET is carried out in an electrolyzer in which a bath filled with electrolyte is the cathode and the workpiece is the anode. When a voltage in the range of 200 to 300 V is applied to the electrolyzer, the electrolyte boils around the anode surface to form a stable electrically conductive vapor–gas envelope. The electrical conductivity of the vapor–gas envelope is lower than that of the electrolyte and metal electrodes. The passage of an electric current through the envelope produces an amount of heat in it sufficient to heat the anode to temperatures from 500 to 1100 °C.

The cylindrical electrolyzer (3 in Figure 1) ensured the circulation of the solution at a constant rate and stabilization of the temperature of the solution. The solution was pumped through a heat exchanger into the cylindrical cathode, and then the solution flowed about the sample anode (1 in Figure 1) and then overflowed into the pan, from where it entered the pump.

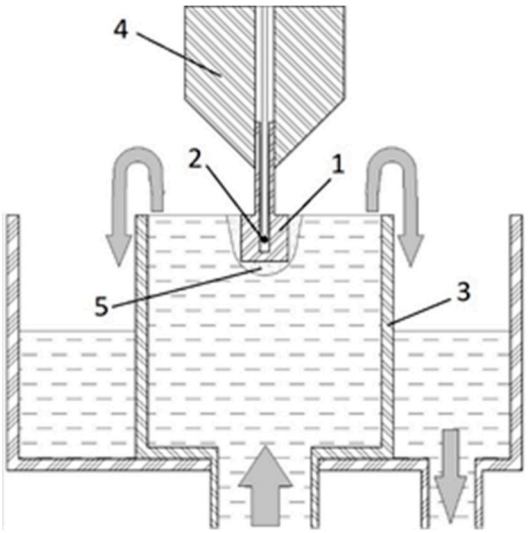

Figure 1. Electrolyzer scheme: 1—sample anode, 2—thermocouple, 3—cathode, 4—current supply and sample mounting system, 5—vapor–gas envelope.

Structural low-carbon steel (0.17–0.24 C, 0.17–0.37 Si, 0.35–0.65 Mn, Ni $\leq$ 0.25, S $\leq$ 0.04, P $\leq$ 0.04, Cr $\leq$ 0.25, Cu $\leq$ 0.25, As $\leq$ 0.08, and the rest Fe) was used for treatment. Cylindrical samples with a diameter of 11 mm and a height of 15 mm were subjected to PES. The flow rate of the solution was measured with a rotameter (accuracy = 2.5%). The temperature of the solution at the outlet of the heat exchanger was measured with an MS6501 multimeter (Precision Mastech Enterprises, Hong Kong) using a chromel–alumel thermocouple (accuracy = 3%) and maintained at 20 $\pm$ 1 °C.

The samples were connected to the positive output of the power supply, and the electrolyzer was connected to the negative output. After voltage was applied to the system, the samples were immersed in the electrolyte to a depth equal to their height. The voltage was measured with an LM-1 voltmeter (United Era, Poland) (accuracy $\pm$ 0.5%), and the current was measured with an MS8221 multimeter (Precision Mastech Enterprises, Hong Kong). The sample temperature was measured with the MS8221 multimeter using

the M89-K1 thermocouple with an accuracy of 2% in the temperature range from 400 to 1000 °C. The thermocouple was placed in an axial hole in the sample and was in direct contact with the sample at a point 2 mm away from its lower end. The treatment time was 5 and 10 min, and then the samples were quenched from the treatment temperature. Quenching was carried out by disconnecting the voltage, which caused the collapse of the vapor–gas envelope and the restoration of the contact of the sample with the cooled electrolyte.

An aqueous electrolyte of the following composition was used: 10% (wt.) ammonium sulfate $(NH_4)_2SO_4$, 10% (wt.) dimethyl sulfoxide $(CH_3)_2SO$. The treatment temperature varied from 500 to 900 °C in increments of 50 °C. Part of the samples of the control group was treated for 5 min at a temperature of 750 °C in an aqueous electrolyte of the following composition: 10% (wt.) ammonium chloride NH_4Cl, 20% (wt.) carbamide $(CO(NH_2))_2$.

2.2. Surface Characterization

Friction tests were carried out according to the "shaft–pad" scheme (Figure 2). The cylindrical sample was mounted on a shaft driven by an electric motor. A counter body, which was a plate 2 mm thick with a semicircular notch on one of the edges, was pressed against the generatrix of the cylindrical sample. The counter body notch had a radius of 5 mm and tightly covered the surface of the sample. Thus, during the wear of the friction pair, the contact area of the friction pair practically did not change. The counter body was fixed on a movable table, and it was pressed against the sample by the piston rod of a pneumatic cylinder. The air pressure in the cylinder determined the force with which the counter body was pressed against the sample. The counter body, together with the cylinder and the table, was mounted on a crank, which had the ability to rotate coaxially with the cylindrical sample. During testing, the crank remained immobile because it was connected to a strain gauge that restricted the movement of the crank. The strain gauge signal allowed determining the moment of friction force. Another strain gauge was connected to a movable table and was intended to measure the force with which the counter body was pressed against the sample. An infrared pyrometer was used to measure the temperature on the friction track at the exit point of the track from the contact zone of the sample and the counter body.

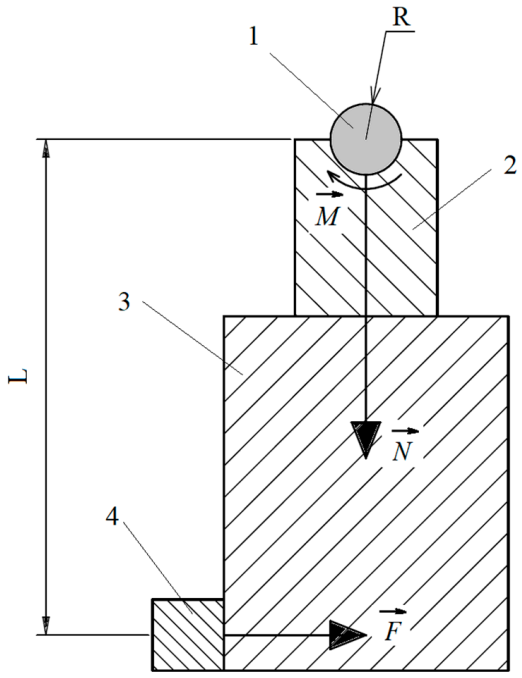

Figure 2. Friction test scheme. 1—cylindrical sample; 2—counter body; 3—crank; 4—strain gauge.

The friction machine was manufactured by Kostroma State University (patent RU 213413 U1).

The phase composition was determined using an Empyrean X-ray diffractometer manufactured by Panalytical using Co-Kα cobalt radiation (Panalitical, Espoo, Finland).

The microhardness of the surface layer of the samples was measured using a Falcon 500 microhardness meter (Innovatest, Maastricht, The Netherlands).

A solution of nitric acid in ethyl alcohol was used to etch the surface of the metallographic specimen. Immediately afterward, a solution of the following composition was used: sodium thiosulfate (24 g), citric acid (3 g), plumbic acetate (2.5 g), and sodium nitrite (0.25 g) per 100 mL of distilled water. The second solution was required for the rapid identification of the sulfide inclusions.

The TESCAN VEGA 3 scanning electron microscope (Tescan Vega3, Brno, Czech) was used to obtain images of the surface of the treated samples. Determination of the concentration distribution of sulfur, carbon, nitrogen, and oxygen on the modified surface was performed by EDX analysis on the same microscope.

The characteristics of the microgeometry of the friction track surface were studied on the TR-200 profilometer (Time Group Inc., Beijing, China).

The scratch test was carried out on a Nanovea device according to the method from the ASTM C1624-05 standard [22]. The indenter was a diamond cone with an angle at the top of 120° and a radius of rounding of the top of 100 μm. The tests were carried out with a load linearly increasing from 0.2 to 40 N. The loading speed during the tests ranged from 1 to 3 N/min.

2.3. Calculation of the Wear Mechanism

To analyze the experimental dependences obtained, it is necessary to establish the mechanism of friction surface destruction and the type of friction bond breaking. For this purpose, the value of the relative penetration of the irregularities of the pressed surfaces of the friction pair h/r (r is the radius of the irregularity, h is the depth of its penetration into the surface of the solid) and the shear strength of molecular bonds relative to the material yield point $\frac{\tau}{\sigma_T}$ were determined. According to [19], for steels, friction bonds are broken as a result of elastic displacement of the material at values $h/r < 0.01$. Plastic displacement of the material is characterized by residual deformation of the surface after the passage of micro-irregularities and occurs during dry friction when $h/k < 0.1$. Values of $h/k > 0.1$ lead to micro-cutting, characterized by the formation of micro-chips.

The mathematical model used for calculations is based on the values of parameters determined experimentally on friction tracks using a profilometer. Thus, the resulting model relations obtained are close to those that actually take place.

Modeling of the sample surface irregularities by bodies of double curvature gives the following expression for the average radius of a single micro-irregularity [23]:

$$r = \frac{9R_a^2 S_m^2}{128\left(5,5R_a - R_p\right)^3}, \quad (1)$$

where R_a is the arithmetical average roughness; R_p is the smoothing height or the distance from the line of protrusions to the center line within the base length l. The line of protrusions is drawn through the top of the highest irregularity parallel to the center line; S_m is the mean spacing between peaks. The numerical values of the values R_a, R_p, and S_m are obtained by direct measurements with a profilometer on the friction tracks of the sample and the counter body. The values of the radii of micro-irregularities (1) were averaged on the basis of 30 profilograms.

Next, we find the depth of the penetration of a single micro-irregularity into the surface of the counter body. To do this, we need an analytical expression for the curve of the support surface or a function of the material distribution over the height of the rough layer.

Let us define this function as:

$$\eta = t_m\left(\frac{z}{R_p}\right)^{\nu} = b\left(\frac{z}{R_{\max}}\right)^{\nu} = b\varepsilon_{\max}^{\nu} = \frac{A_r}{A_c} = \frac{P_c}{P_r}, \quad (2)$$

where z is the profile section level measured from the ledge line, $R_{\max}$ is the maximum height of profile irregularities, $\varepsilon_{\max} = z/R_{\max}$ is relative profile asperity, ν and b are parameters of the distribution function (2), P_r is the average real pressure at the friction contact, A_r is the actual contact area, P_c is the contour pressure, and A_c is the contour contact area.

Values of the parameters v and b are a result of friction track profilogram processing [24]:

$$\nu = 2t_m\left(\frac{R_p}{R_a}\right) - 1, \quad (3)$$

$$b = t_m\left(\frac{R_{\max}}{R_p}\right)^{\nu}, \quad (4)$$

where t_m is the relative length of the profile at the center line level.

$$t_m = \frac{\sum_1^n \Delta l_i}{l}, \quad (5)$$

where l is the base length and $\sum_1^n \Delta l_i$ is the sum of the lengths of the segments cut off by the center line in the profile.

The parameter t_m is determined by direct measurements of the profilometer on the friction tracks of both the test sample and the counter body.

Expressions (2)–(4) are used for the case of contact of a rough surface with a smooth one.

The surfaces of the sample and the counter body are similar in hardness and, in addition, have a roughness of the same order; therefore, we apply the equivalent Demkin material distribution function reflecting the microgeometry of both surfaces, having performed calculations similar to [25].

The distribution function of the material over the height of the rough layer on the friction tracks of the sample is designated as η_1, and that of the counter body is designated as η_2. Similarly, all parameters related to the surface of the sample will be numbered with index 1, and those related to the surface of the counter body will be numbered with index 2.

$$\eta_1(z_1) = b_1\left(\frac{z_1}{R_{\max 1}}\right)^{\nu_1}, \quad (6)$$

$$\eta_2(z_2) = b_2\left(\frac{z_2}{R_{\max 2}}\right)^{\nu_2}. \quad (7)$$

The material distribution function is formed by combining the distribution laws of the sample material (index 1) and the counter body (index 2) using the Kragelsky method.

$$\begin{aligned}\eta = \frac{b_1 b_2}{R_{\max 1}^{\nu_1} R_{\max 2}^{\nu_2}}\cdot\left(1 - \frac{\nu_2\nu_1}{(\nu_2+1)} + \frac{\nu_2\nu_1(\nu_1-1)}{2(\nu_2+2)} - \frac{\nu_2\nu_1(\nu_1-1)(\nu_1-2)}{6(\nu_2+3)} + \frac{\nu_2\nu_1(\nu_1-1)(\nu_1-2)(\nu_1-3)}{24(\nu_2+4)}\right)\\ \cdot(R_{\max 1}+R_{\max 2})^{\nu_1+\nu_2}\cdot\left(\frac{h}{R_{\max 1}+R_{\max 2}}\right)^{\nu_1+\nu_2} = \frac{b_1 b_2}{R_{\max 1}^{\nu_1} R_{\max 2}^{\nu_2}}\cdot\left(1 - \frac{\nu_2\nu_1}{(\nu_2+1)} + \frac{\nu_2\nu_1(\nu_1-1)}{2(\nu_2+2)}\right.\\ \left. - \frac{\nu_2\nu_1(\nu_1-1)(\nu_1-2)}{6(\nu_2+3)} + \frac{\nu_2\nu_1(\nu_1-1)(\nu_1-2)(\nu_1-3)}{24(\nu_2+4)}\right)\cdot(R_{\max 1}+R_{\max 2})^{\nu_1+\nu_2}\cdot\varepsilon^{\nu_1+\nu_2} = b_{1,2}\cdot\varepsilon_{\max}^{\nu_1+\nu_2},\end{aligned} \quad (8)$$

where the designation is entered,

$$\varepsilon = \frac{h}{R_{\max 1} + R_{\max 2}}. \tag{9}$$

Equation (8) is an expression of the reference curve of some rough surface equivalent to the considered two rough surfaces of the counter body and the sample.

Expression (8) is structurally similar to expression (2) if we assume that the distribution parameter $\nu_{1,2}$ of the equivalent reference curve is the sum of the parameters of the sample ν_1 and the counter body ν_2:

$$\nu_{1,2} = \nu_1 + \nu_2. \tag{10}$$

The maximum height of the irregularities of the equivalent profile $R_{\max 1,2}$ is determined by the sum of the maximum heights of the irregularities of the sample and the counter body:

$$R_{\max 1,2} = R_{\max 1} + R_{\max 2}. \tag{11}$$

The expression is used as the smoothing height $R_{p1,2}$ of the equivalent reference curve:

$$R_{p1,2} = R_{p1} + R_{p2}. \tag{12}$$

Expression (2) for $z = h$ for the parameters of the distribution of the equivalent curve has the following form:

$$\eta = b_{1,2}\left(\frac{h}{R_{\max 1} + R_{\max 2}}\right)^{\nu_1+\nu_2} = \frac{P_c}{P_r}. \tag{13}$$

Then the absolute convergence of the surfaces will be equal to

$$h = (R_{\max 1} + R_{\max 2})\left(\frac{P_c}{b_{1,2}P_r}\right)^{\frac{1}{\nu_1+\nu_2}}, \tag{14}$$

where the coefficient $b_{1,2}$ is given by the expression

$$b_{1,2} = \frac{b_1 b_2 (R_{\max 1} + R_{\max 2})^{\nu_1+\nu_2}}{R_{\max 1}^{\nu_1} R_{\max 2}^{\nu_2}} \cdot \left(1 - \frac{\nu_2\nu_1}{(\nu_2+1)} + \frac{\nu_2\nu_1(\nu_1-1)}{2(\nu_2+2)} - \frac{\nu_2\nu_1(\nu_1-1)(\nu_1-2)}{6(\nu_2+3)} + \frac{\nu_2\nu_1(\nu_1-1)(\nu_1-2)(\nu_1-3)}{24(\nu_2+4)}\right). \tag{15}$$

To calculate the actual pressure at the tops of the micro-irregularities P_r, in Expression (14) we define the type of contact: elastic or plastic.

Deformations of rubbing surfaces will be elastic if the applied load and the force of molecular interaction do not lead to stresses in the surface layer exceeding the yield strength of the steel sample.

Plastic contact is realized when the contact stresses at the friction unit exceed the yield strength of the sample material, which leads to the penetration of the rough surface irregularities of a harder body into a surface with less hardness.

The Williamson–Greenwood criterion, also called the plasticity index, has become the most widespread [26,27].

$$K_p = \frac{\Theta}{HB}\sqrt{\frac{R_p}{r}}, \tag{16}$$

where Θ is the reduced modulus of elasticity:

$$\Theta = \left(\frac{1-\mu_1^2}{E_1} + \frac{1-\mu_2^2}{E_2}\right), \tag{17}$$

where ${\mu^2}_i$ and E_i are Poisson's coefficients and elastic moduli of interacting bodies.

The dimensionless parameter K_p describes the deformation properties of a rough surface. If the value of this parameter is much less than 1, then the deformations of irregularities in contact with a flat surface will be completely elastic, if the value exceeds 1, then the deformations will be predominantly plastic.

In the case under consideration, the plasticity index is greater than 6 in the entire range of changes in the sliding velocities of the sample along the counter body; therefore, the contact is plastic. In the case of plastic deformation, we assume the stress on the contact to be equal to the hardness, according to [27]: $p_r \approx HB$. The applied load N sets the contour pressure.

Thus, the expression for absolute penetration will take the following form:

$$h = (R_{\max 1} + R_{\max 2}) \left(\frac{N}{b_{1,2} HB} \right)^{\frac{1}{\nu_1 + \nu_2}}. \quad (18)$$

The relative penetration of the irregularities of the friction surfaces is defined as the ratio of the absolute penetration (28) to the average radius of the micro-irregularities (1):

$$\frac{h}{r_{1,2}} = \frac{(R_{\max 1} + R_{\max 2})}{r_{1,2}} \cdot \left(\frac{N}{b_{1,2} \cdot HB} \right)^{\frac{1}{\nu_1 + \nu_2}}, \quad (19)$$

where $r_{1,2}$ is the reduced radius, determined according to [24]:

$$r_{1,2} = \frac{r_1 r_2}{r_1 + r_2}. \quad (20)$$

In addition, to characterize the operational properties of the surface, we calculate the dimensionless Kragelsky criterion:

$$\Delta = \frac{R_{\max}}{r b^{\frac{1}{\nu}}}. \quad (21)$$

The complex (21) is the most complete roughness evaluation including not only geometric but also statistical characteristics of the distribution of irregularities in height, as well as the average radius of micro-irregularities. The physical essence of the parameter Δ is to determine the bearing capacity of the roughness profile.

3. Results

3.1. Temperature–Voltage and Current–Voltage Characteristics of PES

Figures 3 and 4 show the temperature–voltage and current–voltage characteristics of PES in an electrolyte with the addition of dimethyl sulfoxide. The temperature increases with increasing voltage due to an increase in the input power and reaches a maximum of 900 °C at a voltage of 220 V. The maximum on the temperature–voltage curve determines the maximum achievable treatment temperature in this electrolyte for the samples with a surface area of 260 mm^2. The current decreases with increasing voltage due to an increase in the thickness of the vapor–gas envelope with increasing voltage, which is typical for PET.

3.2. Structure, Elemental Composition, and Phase Composition of the Surface Layer after PES

EDX analysis shows the enrichment of the surface layer of the samples with sulfur, carbon, nitrogen, and oxygen at all treatment temperatures (Figure 5). The carbon content in the surface layer decreases as the treatment temperature increases due to the decarburizing process. The electrolyte with ammonium sulfate creates conditions for the diffusion of nitrogen into the surface layer. The sulfur content is maximum at a treatment temperature of 500 °C and gradually decreases with increasing PES temperature. According to X-ray diffraction data, the surface layer contains iron oxides and sulfides (Figure 6).

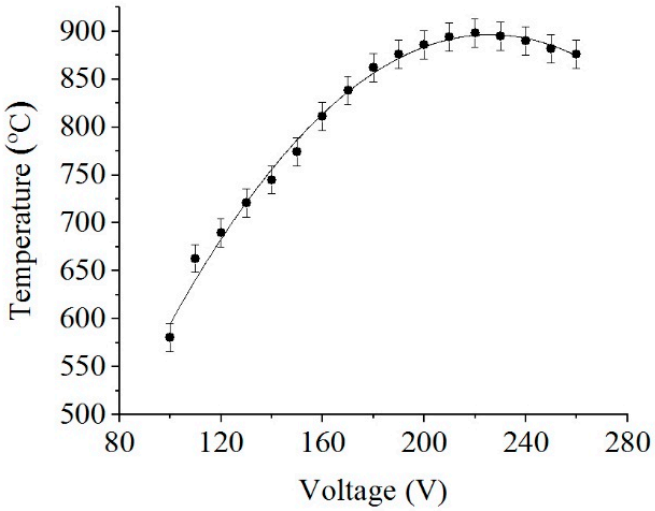

Figure 3. Temperature–voltage characteristic of PES.

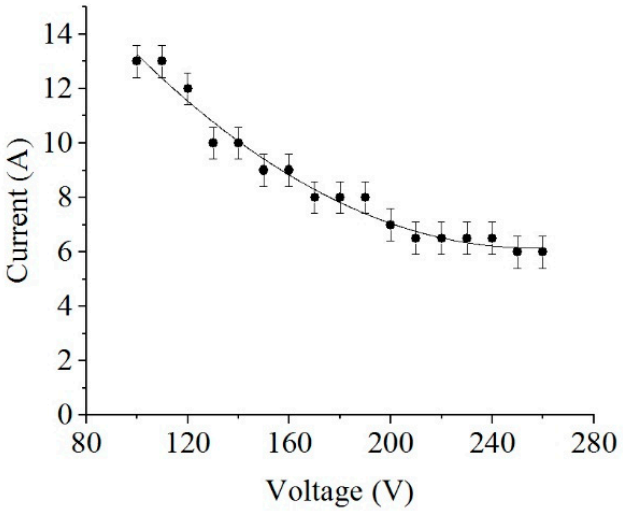

Figure 4. Current–voltage characteristic of PES.

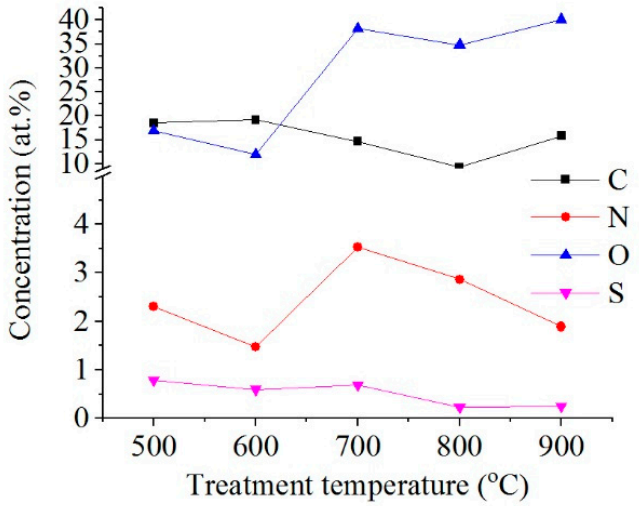

Figure 5. Dependence of the surface concentration of carbon, nitrogen, oxygen, and sulfur on the PES temperature.

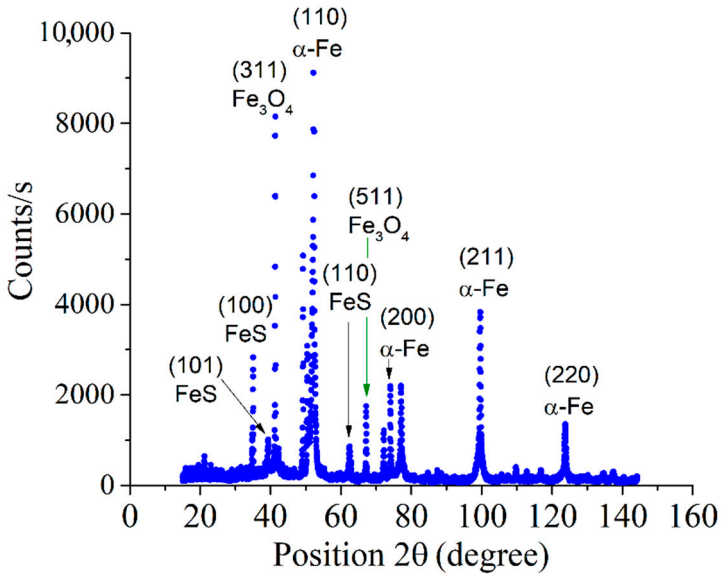

Figure 6. X-ray diffraction patterns of the steel surface layer after PES at 750 °C.

The oxygen content increases with increasing treatment temperature from 16.9 at.% at 500 °C up to 40.1 at.% at 900 °C (Figure 5), but it is not enough for the formation of a continuous oxide layer (Figure 7).

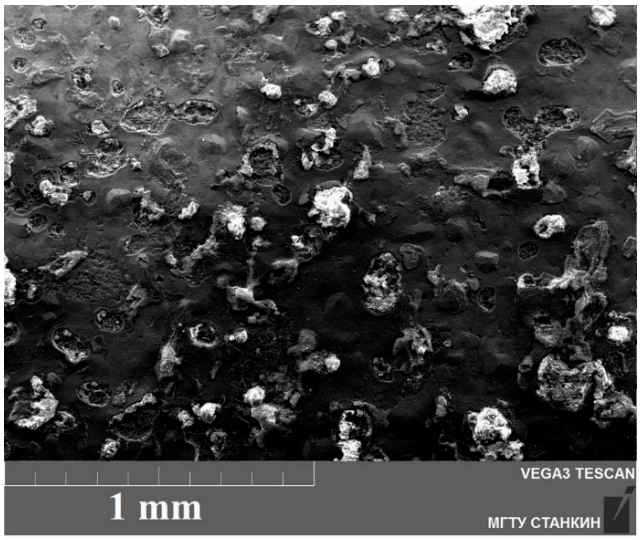

Figure 7. SEM images of the steel surfaces after PES at 700 °C.

A mechanical mixture of iron and Fe_3O_4 oxides is formed on the steel surface, with inclusions of FeO due to the processes of high-temperature oxidation of iron in water vapor and electrochemical oxidation in the process of charge transfer by electrolyte anions [28]. The outer layer contains pores (Figure 7), which facilitate the diffusion of sulfur, carbon, and nitrogen into the material, in addition to the existing vacancies [29].

Metallographic analysis of the surface layer shows the formation of two zones (Figure 8). The zone enriched in iron sulfides has the greatest thickness of about 0.2 mm after treatment at 500–600 °C. As the temperature rises, the thickness of this zone decreases to 0.06 mm after saturation at 850–900 °C. Zone I after treatment at temperatures of 600–900 °C is followed by a hardened zone as a result of the formation of hardening martensite. The value of microhardness increases with an increase in the treatment temperature (Figure 9).

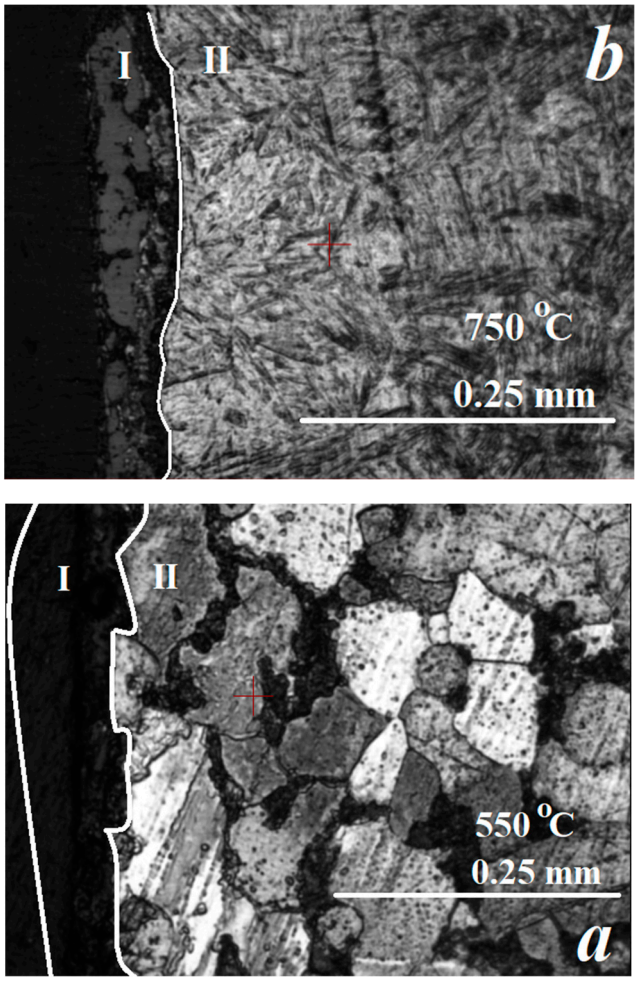

Figure 8. Microstructure of the cross-section of the steel surface after PES at a temperature of 550 °C (**a**) and 750 °C (**b**). I—zone enriched with iron sulfides, II—ferrite-perlite mixture (**a**), hardening zone containing martensite (**b**).

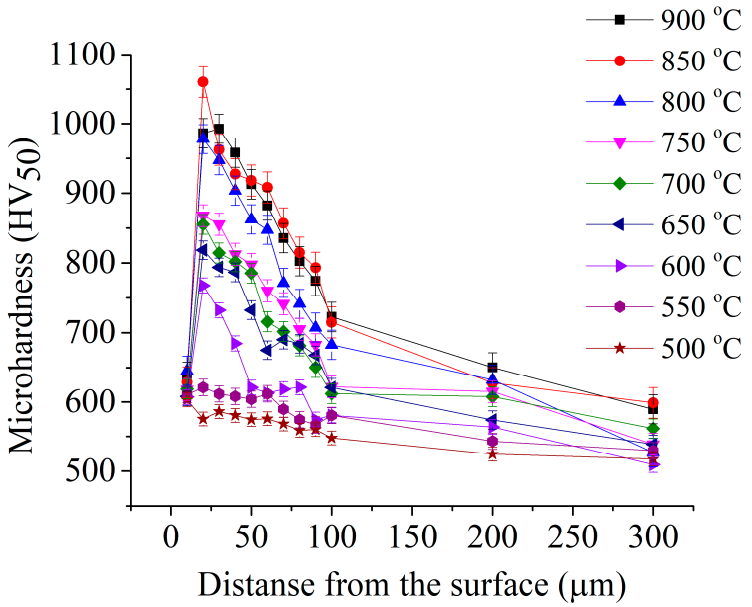

Figure 9. Microhardness distribution in the surface layer after PES at different temperatures.

3.3. Friction and Wear Characteristics

The calculation of the relative penetration values shows that friction bonds are broken due to plastic displacement of the material during plastic flow around the deforming protrusion (Table 1). A roller of deformable material is formed in front of the protrusion, and the material is pushed aside at the edges. The friction surfaces are characterized by residual deformation after the passage of the micro-irregularities. With this type of stress state, low-cycle frictional fatigue occurs in the surface layer of the sample.

Table 1. Relative penetration at different treatment temperatures and times.

T (°C)	500	550	600	650	700	750	800	850	900
					5 min treatment				
h/r	0.048	0.046	0.051	0.050	0.052	0.066	0.072	0.074	0.089
					10 min treatment				
h/r	0.042	0.050	0.048	0.052	0.058	0.062	0.071	0.068	0.079

During plastic contact, the force expended on the surface layer deformation is due to the resistance of the material of the deformable sample to plastic displacement and the formation of a friction track. Friction tracks with traces of plastic deformation of sulfided samples are shown in Figure 10.

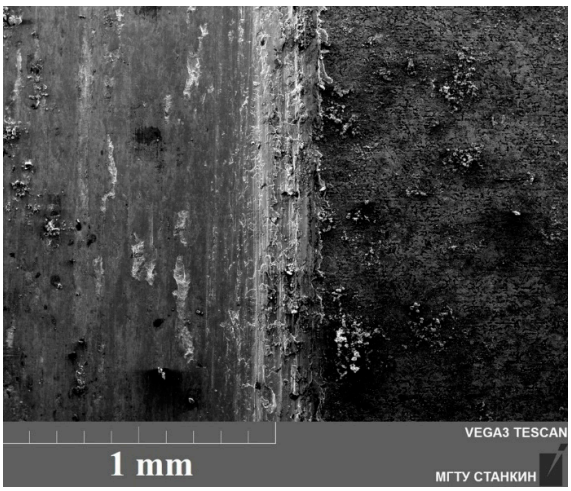

Figure 10. SEM image of wear tracks of the surface sulfided at 500 °C for 5 min. The friction distance is 1 km, the sliding speed is 1.555 m/s, and the load is 10 N.

The scratch test under a load linearly increasing from 0.2 to 40 N was carried out for samples sulfided at temperatures of 550, 650, 750, and 850 °C. On each sample, two tests were carried out, one directly on the friction track after 1 km of tests, and the other on a modified surface that was not subjected to tribological tests. The destruction of the modified layer on the surface without a friction track is accompanied by plastic deformation, chips, and cracks of the oxide layer on the surface. On the friction paths of all samples, only areas of plastic deformation are observed (Figure 11).

Figure 11. Panorama of a scratch on the friction track of a sample sulfided at 550 °C for 5 min. The friction distance is 1 km, the sliding speed is 1.555 m/s, and the load is 10 N.

Thus, the wear mechanism of samples sulfided at all temperatures is fatigue wear during dry friction and plastic contact.

According to Figures 12 and 13, in the first few minutes of friction, the running-in of the friction pair occurs. A new relief is formed on the friction tracks, which is characteristic of the given specific loading conditions and the sliding speed of the sample over the counter body. Under these conditions, the changes in the friction coefficient and the average bulk temperature in the surface layer of the sample over the time of the tribological test are small. As can be seen in Figure 13, after sulfiding, there is a greater decrease in the friction coefficient than after nitrocarburizing the same steel.

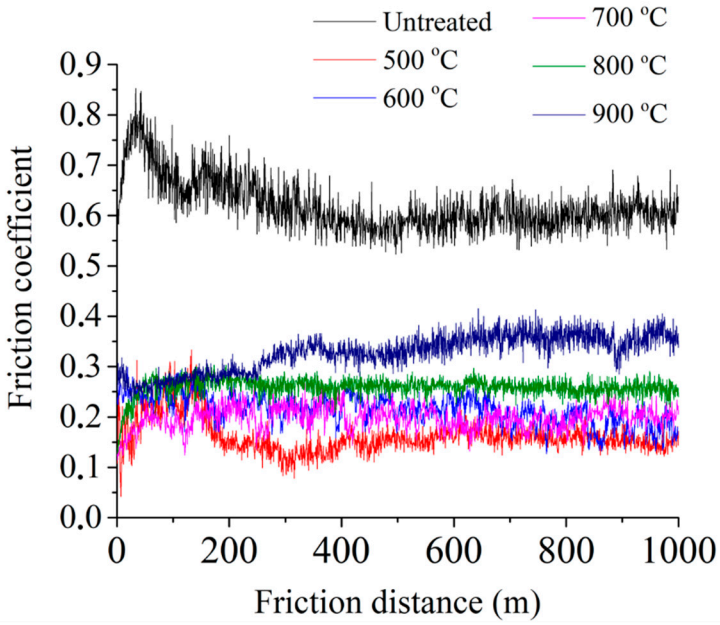

Figure 12. The dependence of the friction coefficient on the friction distance for samples sulfided at different temperatures for 5 min and for an untreated sample. The friction distance is 1 km, the sliding speed is 1.555 m/s, and the load is 10 N.

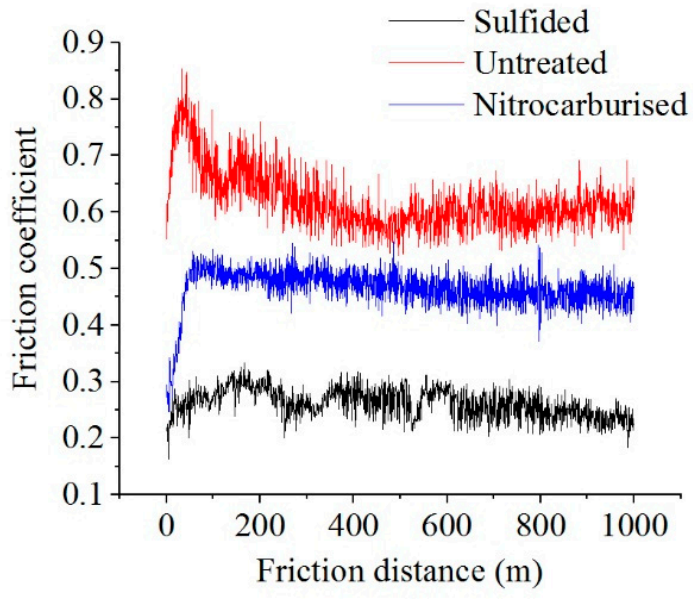

Figure 13. The dependence of the friction coefficient on the friction distance for samples sulfided at 750 °C for 5 min, an untreated sample, and a sample nitrocarburized at 750 °C for 5 min. The friction distance is 1 km, the sliding speed is 1.555 m/s, and the load is 10 N.

Variation of the temperature and duration of sulfiding showed that the greatest decrease in the friction coefficient occurs at the minimum treatment temperature (Figure 14). Increasing the duration of PES from 5 to 10 min also helps to reduce the friction coefficient. The greatest decrease (by 5.5 times) in the average value over the last 100 m of the friction coefficient occurs after sulfiding at 500 °C for 10 min compared to the untreated sample. An increase in the friction distance to 2 km leads to an increase in the friction coefficient by 1.05–1.25 times.

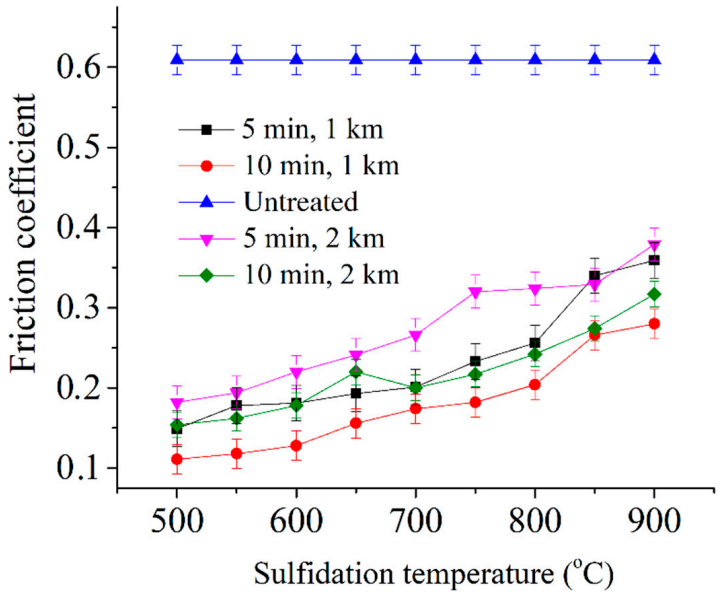

Figure 14. Dependence of the friction coefficient averaged over the last 100 m on the sulfidation temperature at different treatment times. The friction distance is 1 and 2 km, the sliding speed is 1.555 m/s, and the load is 10 N.

Similar dependences are observed with the weight wear of samples (Figure 15).

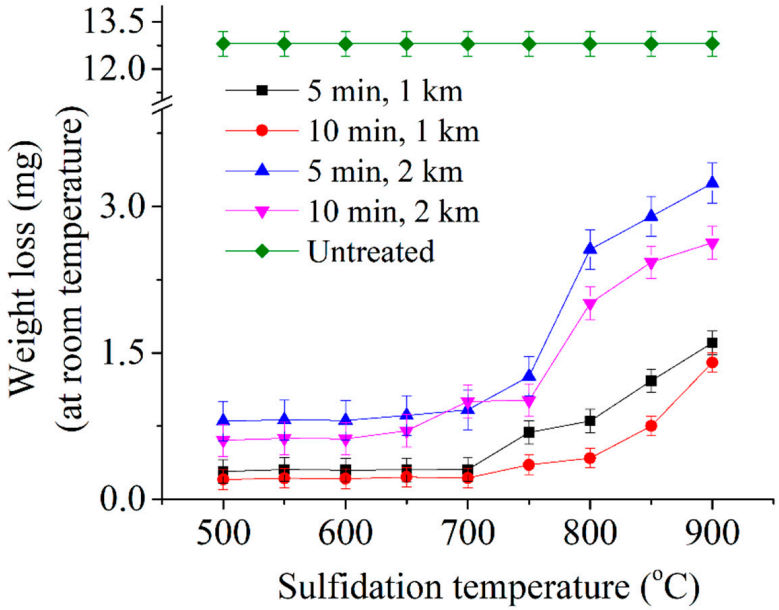

Figure 15. Dependence of the weight loss during the friction tests on the sulfidation temperature at different treatment times. The friction distance is 1 and 2 km, the sliding speed is 1.555 m/s, and the load is 10 N.

The smallest weight wear is observed after PES at 500 °C for 10 min, which is 64 times lower than that of the untreated sample. It is also shown that the mass wear of sulfided samples is 6.2 times lower than that of nitrocarburized samples (Figure 16), which is clearly reflected in the profile of friction tracks (Figure 17).

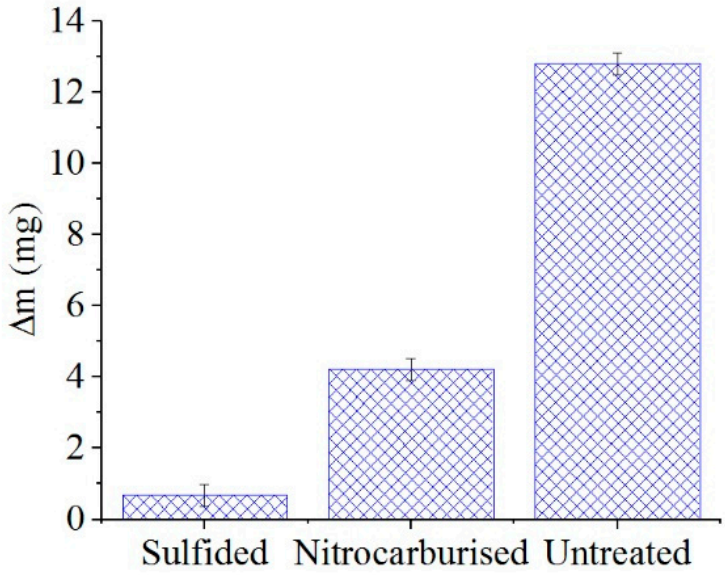

Figure 16. Weight loss during friction of sulfided and nitrocarburized samples at 750 °C for 5 min and untreated sample. The friction distance is 1 km, the sliding speed is 1.555 m/s, and the load is 10 N.

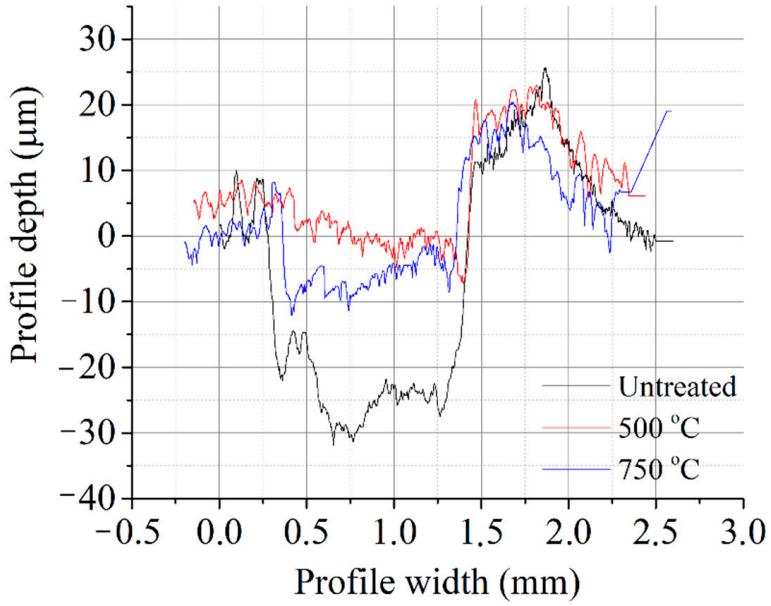

Figure 17. Profile of the friction tracks on samples sulfided at 500 and 750 °C for 5 min and on an untreated sample. The friction distance is 1 km, the sliding speed is 1.555 m/s, and the load is 10 N.

An increase in the treatment temperature leads to an increase in the Kragelsky–Kombalov criterion Δ on the friction tracks at any treatment time (Figure 18). After 1 km of testing, the increase in the Kragelsky–Kombalov criterion for higher treatment temperatures is more intense than that after 2 km. In the first case, Δ grows according to a parabolic law; after 2 km of testing, the growth becomes linear. Longer saturation provides a decrease in Δ both after 1 and after 2 km of friction.

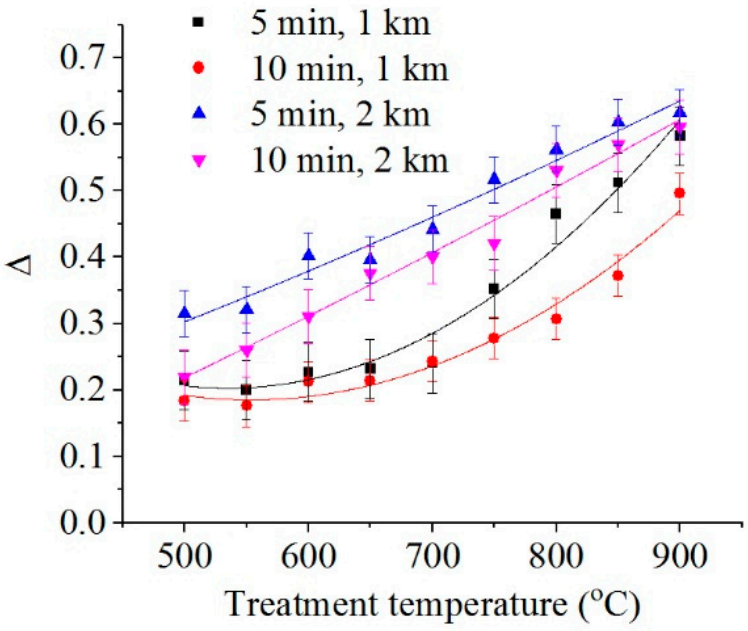

Figure 18. Dependence of the Kragelsky–Kombalov criterion Δ on the treatment temperature at different treatment times. The friction distance is 1 and 2 km, the sliding speed is 1.555 m/s, and the load is 10 N.

Temperature measurement in the tribological contact zone showed that an increase in the treatment temperature leads to an increase in this friction parameter (Figure 19).

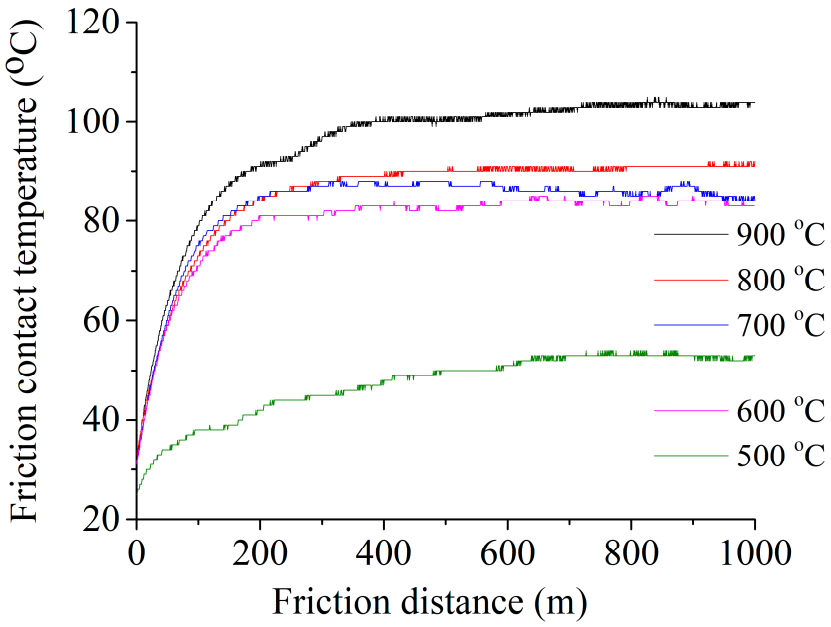

Figure 19. Dependence of the temperature in the tribological contact zone on the friction distance for samples sulfided at different temperatures. The sliding speed is 1.555 m/s; the load is 10 N.

An increase in the sliding speed of the sample along the counter body from 0.52 to 10.36 m/s leads to a decrease in the relative penetration of irregularities (Figure 20), the friction coefficient (Figure 21), the complex roughness criterion Δ (Figure 22), and weight wear (Figure 23).

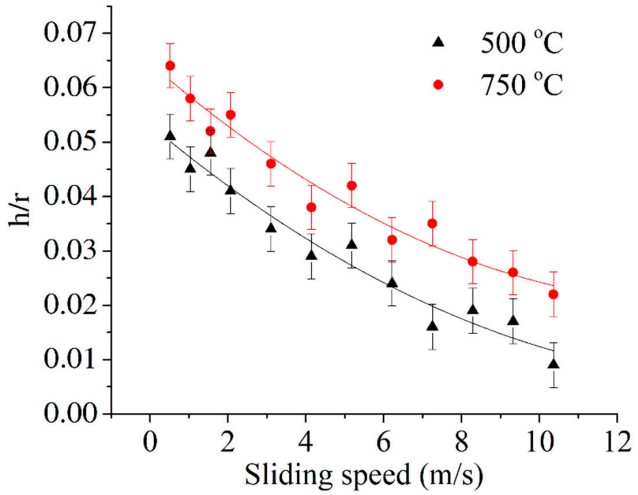

Figure 20. Dependence of relative approach on the sliding speed. The friction distance is 1 km; the load is 10 N.

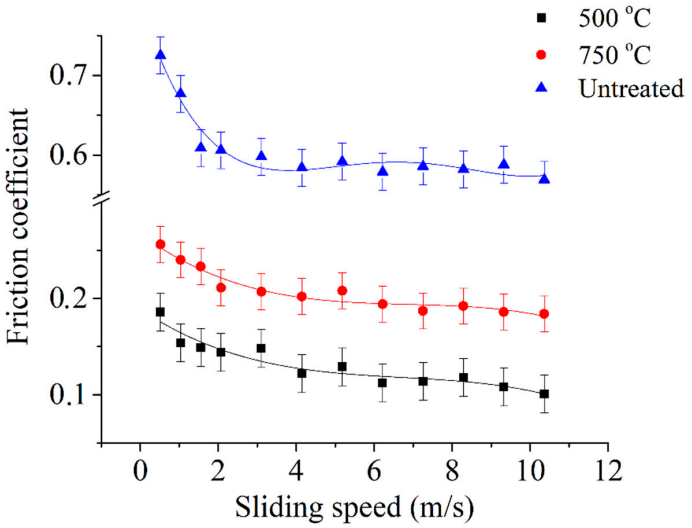

Figure 21. Dependence of the friction coefficient averaged over the last 100 m on the sliding speed. The friction distance is 1 km; the load is 10 N.

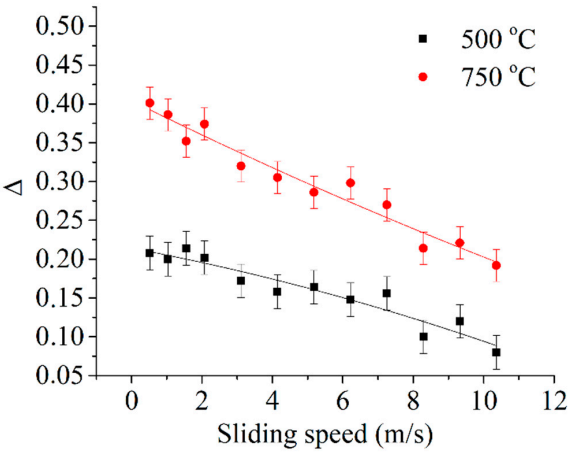

Figure 22. Dependence of the Kragelsky–Kombalov criterion Δ on the sliding speed. The friction distance is 1 km, the load is 10 N.

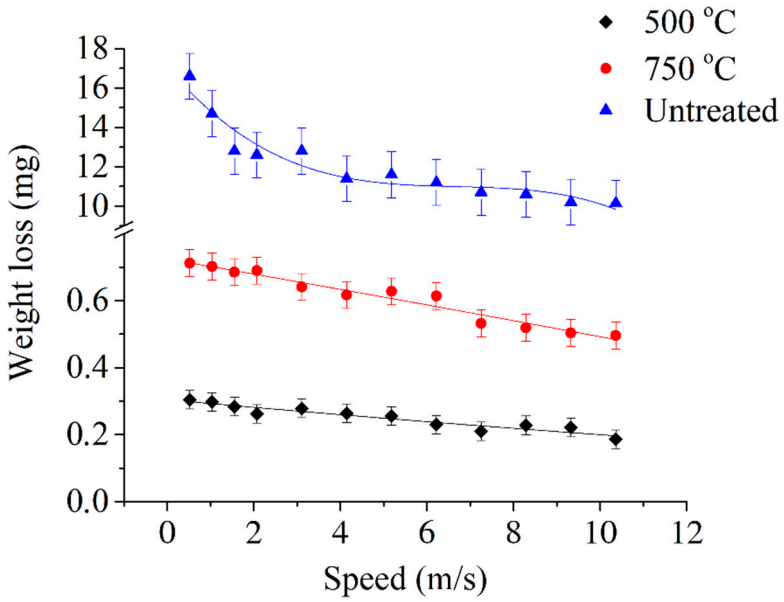

Figure 23. Dependence of the weight loss during the friction tests on the sliding speed. The friction distance is 1 km; the load is 10 N.

4. Discussion

From the obtained characteristics of sample heating in electrolysis plasma, it follows that treatment in a solution of ammonium sulfate and dimethyl sulfoxide has typical temperature–voltage and current–voltage characteristics for anodic plasma electrolytic treatment, which makes it possible to vary the treatment temperature by voltage regulation.

The result of heating and holding steel specimens at temperatures that ensure diffusion processes is the formation of a modified surface layer. This layer consists of a mixture of iron oxides as a result of high-temperature oxidation, iron sulfide as a result of sulfur diffusion, and a solid solution of nitrogen and carbon forming quench martensite as a result of nitrogen diffusion. Nitrogen diffusion provides strengthening of the modified layer, and the value of microhardness is determined by the hardening temperature (hardening was carried out from the diffusion saturation temperature), as well as the concentration of nitrogen and carbon.

The diffusion of sulfur can be associated with the emission of sulfate ions on the anode sample, as well as the adsorption of dimethyl sulfoxide molecules, followed by the decomposition of chemical compounds to the atomic state. Nitrogen diffuses into steel in atomic form after adsorption on the sample surface of ammonia molecules formed during the hydrolysis of ammonium ions.

The larger radius of the sulfur atom compared to the atoms of the other diffusants does not allow sulfur to diffuse to a greater depth. This leads to competition between sulfur and oxygen in the near-surface layer for interaction with iron and the formation of chemical compounds with it. The result of this is the prevalence of sulfur diffusion at low temperatures, when high-temperature oxidation proceeds less intensively.

The formation of a modified layer, which consists of oxides and sulfides of iron in the near-surface layer and a hardened substrate, determines the wear mechanism as fatigue wear during dry friction and plastic contact under the conditions of tribological tests. A favorable effect of iron sulfides on reducing the coefficient of friction and weight wear is shown, both with varying PES conditions (with a decrease in treatment temperature and an increase in treatment time) and when compared with nitrocarburizing of the same steel grade under similar treatment conditions.

A comprehensive assessment of the quality of the surface layer is given by the Kragelsky–Kombalov criterion Δ. According to the molecular mechanical theory of wear under plastic deformations in the zones of actual contact, the molecular component of

the coefficient of external friction does not depend on the microtopography of surfaces. The deformation component increases with the increase in the complex Δ. Thus, the total coefficient of external friction increases with increasing criterion Δ. Large values of the Kragelsky–Kombalov criterion were obtained on samples sulfided at higher temperatures (Figure 18), and the friction coefficient, in accordance with the molecular mechanical theory of wear, should increase, which is shown in Figures 12 and 14.

Comparison of Figures 12–14 with Figures 15–17 shows that with increasing treatment temperature, the friction coefficient increases, as does weight wear, and the profiles of the friction tracks become deeper.

Increasing the treatment temperature leads to a significant increase in hardness. The thickness of the layer enriched with iron sulfides, the relative amount of sulfides in the layer, and the sulfur content in the surface, on the contrary, decrease with increasing treatment temperature. The results obtained show that the leading parameter for increasing the wear resistance and frictional properties of low-carbon steel under the studied conditions of tribological tests is not the hardness of the modified layer, but the thickness of the sulfide zone and the relative amount of FeS in it. The sulfide-enriched layer improves surface properties and acts as a permanent lubricant during friction. Moreover, Figure 18 clearly shows that the lower the treatment temperature, the lower the Δ and, consequently, the higher the bearing capacity of the roughness on the friction tracks.

An increase in the treatment temperature leads to the heating of the sample in the tribological contact zone. Under plastic deformations in the zone of tribological contact, a stronger influence on the value of the total diffusion coefficient is exerted by its deformation component, rather than the molecular one. An increase in temperature in the tribological unit leads to an increase in the relative penetration, and hence the deformation component of the diffusion coefficient and the entire friction coefficient as a whole (Figures 12 and 14). In addition, an increase in temperature at actual contact spots contributes to the collapse of irregularities, and, consequently, to an increase in the area of their contact with the counter body and an increase in viscous resistance to deformation, which also increases the coefficient of friction.

In plastic contact, the rate of sliding of the sample over the counter body affects the friction through the rate of propagation of plastic deformation. With an increase in the sliding speed of the sample along the counter body, plastic deformation does not have time to spread to a significant depth and is localized in a smaller near-surface volume, and the relative penetration of irregularities and the size and number of friction bonds decrease. As a result, both the molecular and deformation components of the friction coefficient decrease; consequently, the friction coefficient as a whole decreases (Figure 21). An increase in the sliding speed of the sample over the counter body reduces the adhesion strength of friction bonds, leading to a decrease in the height of the deformed bead and smoothing of the friction surface. As a result, the complex roughness criterion Δ decreases with increasing sliding speed (Figure 22), and the smaller it is, the higher the bearing capacity of roughness; therefore, mass wear decreases with increasing sliding speed of the sample over the counter body (Figure 23).

5. Conclusions

1. The principal possibility of saturating low-carbon steel with sulfur in an electrolyte based on ammonium sulfate and dimethyl sulfoxide with the formation of iron sulfide FeS in the surface layer is shown. The maximum sulfur content in the surface layer is reached at a treatment temperature of 500 °C, when the intensity of competing high-temperature oxidation is low.
2. It has been established that the dominant factor in reducing the friction coefficient and weight wear is the thickness of the sulfide zone and the relative amount of FeS in it, and not the microhardness of the diffusion layer. The greatest decrease in the friction coefficient by 5.5 times and weight wear by 64 times occurs after sulfiding at 500 °C for 10 min.

3. It was revealed that the mechanism of wear of sulfided samples is fatigue wear during dry friction and plastic contact. Using the example of varying the sliding speed, it is shown that a decrease in the friction coefficient with an increase in the sliding speed is provided by the localization of plastic deformation in a smaller near-surface volume, and a decrease in weight wear is due to an increase in the bearing capacity of the surface roughness.

Author Contributions: Conceptualization, T.M. and S.K.; methodology, T.M., I.S. and S.K.; validation, S.G.; formal analysis, I.S.; investigation, T.M., P.P. and R.K.; writing—original draft preparation, T.M.; writing—review and editing, I.S. and S.K.; visualization, S.K.; supervision, I.S.; project administration, S.G.; funding acquisition, S.G. All authors have read and agreed to the published version of the manuscript.

Funding: This work was supported financially by the Ministry of Science and Higher Education of the Russian Federation (project No. 0707-2020-0025). The study was carried out on the equipment of the Center of collective use of MSUT "STANKIN" supported by the Ministry of Higher Education of the Russian Federation (project No. 075-15-2021-695 from 26 July 2021, unique identifier RF—-2296.61321X0013).

Data Availability Statement: Not applicable.

Conflicts of Interest: The authors declare no conflict of interest.

References

1. Grigoriev, S.N.; Vereschaka, A.A.; Fyodorov, S.V.; Sitnikov, N.N.; Batako, A.D. Comparative analysis of cutting properties and nature of wear of carbide cutting tools with multi-layered nano-structured and gradient coatings produced by using of various deposition methods. *Int. J. Adv. Manuf. Technol.* **2017**, *90*, 3421–3435. [CrossRef]
2. Apelfeld, A.; Grigoriev, S.; Krit, B.; Ludin, V.; Suminov, I.; Chudinov, D. Improving the stability of the coating properties for group plasma electrolytic oxidation. *Manuf. Lett.* **2022**, *33*, 54–59. [CrossRef]
3. Metel, A.S.; Grigoriev, S.N.; Melnik, Y.A.; Panin, V.V. Filling the vacuum chamber of a technological system with homogeneous plasma using a stationary glow discharge. *Plasma Phys. Rep.* **2009**, *35*, 1058–1067. [CrossRef]
4. Grigoriev, S.N.; Sinopalnikov, V.A.; Tereshin, M.V.; Gurin, V.D. Control of parameters of the cutting process on the basis of diagnostics of the machine tool and workpiece. *Meas. Tech.* **2012**, *55*, 555–558. [CrossRef]
5. Volosova, M.; Grigoriev, S.; Metel, A.; Shein, A. The Role of Thin-Film Vacuum-Plasma Coatings and Their Influence on the Efficiency of Ceramic Cutting Inserts. *Coatings* **2008**, *8*, 287. [CrossRef]
6. Grigoriev, S.N.; Volosova, M.A.; Okunkova, A.A.; Fedorov, S.V.; Hamdy, K.; Podrabinnik, P.A.; Pivkin, P.M.; Kozochkin, M.P.; Porvatov, A.N. Electrical Discharge Machining of Oxide Nanocomposite: Nanomodification of Surface and Subsurface Layers. *J. Manuf. Mater. Process.* **2020**, *4*, 96. [CrossRef]
7. Grigoriev, S.N.; Kondratsky, I.O.; Krit, B.L.; Ludin, V.B.; Medvetskova, V.M.; Morozova, N.V.; Suminov, I.V.; Apelfeld, A.V.; Wu, R.Z. Protective and Thermophysical Characteristics of Plasma-Electrolytic Coatings on the Ultralight Magnesium Alloy. *J. Eng. Mater. Technol.* **2022**, *144*, 021006. [CrossRef]
8. Yerokhin, A.L.; Leyland, A.; Tsotsos, C.; Wilson, A.D.; Nie, X.; Matthews, A. Duplex surface treatments combining plasma electrolytic nitrocarburising and plasma-immersion ion-assisted deposition. *Surf. Coat. Technol.* **2001**, *142–144*, 1129–1136. [CrossRef]
9. Tsotsos, C.; Yerokhin, A.L.; Wilson, A.D.; Leyland, A.; Matthews, A. Tribological evaluation of AISI 304 stainless steel duplex treated by plasma electrolytic nitrocarburising and diamond-like carbon coating. *Wear* **2002**, *253*, 986–993. [CrossRef]
10. Wu, J.; Deng, J.; Dong, L.; Hou, D. Direct growth of oxide layer on carbon steel by cathodic plasma electrolysis. *Surf. Coat. Technol.* **2018**, *338*, 63–68. [CrossRef]
11. Nie, X.; Wang, L.; Yao, Z.C.; Zhang, L.; Cheng, F. Sliding wear behaviour of electrolytic plasma nitrided cast iron and steel. *Surf. Coat. Technol.* **2005**, *200*, 1745–1750. [CrossRef]
12. Skakov, M.; Yerygina, L.; Scheffler, M. Impact of Electrolytic-Plasma Nitriding on 34CrNi1Mo Steel Surface Layer Properties. *Appl. Mech. Mater.* **2015**, *698*, 439–443. [CrossRef]
13. Ioshinori, T. Electrolytic Thermocemical treatment. *Mech. Technol.* **1977**, *25*, 118–119.
14. Hua, X.-Z.; Zhou, L.; Cui, X.; Zou, A.-H.; Xu, W.-B.; Zhou, X.-L. The Effect Of Ammonia Water On The Microstructure And Performance Of Plasma Electrolytic Saturation Nitriding Layer Of 38CrMoAl Steel. *Phys. Proc.* **2013**, *50*, 304–314. [CrossRef]
15. Belkin, P.N.; Pasinkovsky, E.A.; Tkachenko, Y.G.; Faktorovich, A.A.; Yulyugin, V.K. Effect of plasma electrolytic nitriding on the friction characteristics of 40Ch steel. *Surf. Eng. Appl. Electrochem.* **1981**, *4*, 43–45.
16. Kusmanov, S.A.; Smirnov, A.A.; Silkin, S.A.; Belkin, P.N. Increasing wear and corrosion resistance of low-alloy steel by anode plasma electrolytic nitriding. *Surf. Coat. Technol.* **2016**, *307*, 1350–1356. [CrossRef]

17. Kusmanov, S.A.; Dyakov, I.G.; Kusmanova, Y.V.; Belkin, P.N. Surface Modification of Low-Carbon Steels by Plasma Electrolytic Nitrocarburising. *Plasma Chem. Plasma Proc.* **2016**, *36*, 1271–1286. [CrossRef]
18. Taheri, P.; Dehghanian, C.; Aliofkhazraei, M.; Rouhaghdam, A.S. Evaluation of Nanocrystalline Microstructure, Abrasion, and Corrosion Properties of Carbon Steel Treated by Plasma Electrolytic Boriding. *Plasma Process. Polym.* **2007**, *4*, S711–S716. [CrossRef]
19. Kuzenkov, S.E.; Saushkin, B.P. Borating of steel 45 in electrolytic plasma. *Surf. Eng. Appl. Electrochem.* **1996**, *6*, 10–15.
20. Kusmanov, S.A.; Tambovskiy, I.V.; Sevostyanova, V.S.; Savushkina, S.V.; Belkin, P.N. Anode plasma electrolytic boriding of medium carbon steel. *Surf. Coat. Technol.* **2016**, *291*, 334–341. [CrossRef]
21. Tavakoli, H.; Sobhani, M. Morphological and Electrochemical Study of Sulfide/Nitride Nanostructure Deposited Through Pulsed Plasma Electrolysis. *J. Mater. Eng. Perform.* **2017**, *26*, 1657–1663. [CrossRef]
22. *ASTM C1624-05*; Standard Test Method for Adhesion Strength and Mechanical Failure Modes. ASTM International: West Conshohocken, PA, USA, 2010.
23. Matlin, M.M.; Kazankina, E.M.; Kazankin, V.A. Calculation of the actual contact area between a single microasperity and the smooth surface of a part when the hardnesses of their materials are similar. *J. Frict. Wear* **2011**, *32*, 140. [CrossRef]
24. Kragelsky, I.V.; Dobychin, M.N.; Kombalov, V.S. *Friction and Wear Calculation Methods*; Pergamon Press Ltd.: Oxford, UK, 1982. Available online: https://books.google.ru/books?id=QLcgBQAAQBAJ&hl=ru (accessed on 22 October 2013).
25. Demkin, N.B.; Izmailov, V.V. Surface topography and properties frictional contacts. *Trib. Int.* **1991**, *24*, 21–24. [CrossRef]
26. Graenwood, I.A. *Between Rough Surfaces and Flats*; Series E, N 1; ASME: Washington, DC, USA, 1967.
27. Mukhacheva, T.L.; Belkin, P.N.; Dyakov, I.G.; Kusmanov, S.A. Wear mechanism of medium carbon steel after its plasma electrolytic nitrocarburising. *Wear* **2020**, *462–463*, 203516. [CrossRef]
28. Belkin, P.N.; Yerokhin, A.L.; Kusmanov, S.A. Plasma Electrolytic Saturation of Steels with Nitrogen and Carbon. *Surf. Coat. Technol.* **2016**, *307*, 1194–1218. [CrossRef]
29. Kusmanov, S.A.; Kusmanova, Y.V.; Naumov, A.R.; Belkin, P.N. Formation of diffusion layers by anode plasma electrolytic nitrocarburising of low carbon steel. *J. Mater. Eng. Perform.* **2015**, *24*, 3187–3193. [CrossRef]